

# Energy Harvesting by Floating Flaps

José Pedro de Sousa Ferreira

josepedrof@tecnico.ulisboa.pt

*Instituto Superior Técnico, Universidade de Lisboa, Portugal*

November 2017

## Abstract

The increasing demand for energy efficiency have led to the development of an autonomous flap, which encompasses an energy harvesting system to power sensors and actuators that ultimately perform active gust alleviation. In this context, this research presents a novel mechanism for an electromagnetic energy harvesting concept which transforms self-induced aeroelastic oscillations into electricity. The system exploits the benefits of a release mechanism to reduce the electromagnetic and inertial influence on the flap motion, and its feasibility is evaluated using a numerical model, developing an experimental apparatus, and performing an experimental study. As to the numerical model, the onset of flutter of the original system is calculated using the  $p$ - $k$  method, and the energy harvesting potential is determined on a time-domain simulation that accounts for inertial and electromagnetic non-linearities in the aeroelastic response of the system. A 3D-printed aeroelastic model for wind tunnel testing is developed to experimentally evaluate the energy harvesting mechanism. The test campaign is carried out using vibration tests to structurally characterize the model and quantify the mechanism effectiveness, followed by wind tunnel testing. With a weight penalty of 0.6 % when compared to a standard energy harvesting mechanism with a reciprocating shaft, Free-Floating Flaps fitted with the novel mechanism showed a 40 % decrease in structural damping and 45 % increase in power generation. It was also experimentally demonstrated that the onset of flutter is controllable by adjusting the generator external resistance. Future applications of such mechanism in wind turbine rotors are considered, and aircraft applications are also investigated with promising results suggesting substantial fuel savings.

**Keywords:** Aeroelasticity; Electromagnetic Energy Harvesting; Free-Floating Flaps; Wind Tunnel Flutter Testing; 3D Printing.

## 1. Introduction

With the ever-growing demand for energy efficient aeronautical systems, there has been an increased research activity in the search for novel energy harvesting solutions. This is motivated by the increasingly expensive fossil fuels and by the need to reduce operational costs. The potential of renewable energy power generators has seen a marked increase in proposed solutions in the aeronautical industry.

Amongst the wide range of possibilities for energy harvesting, the one that mostly fits aeronautical purposes is harnessing vibrations induced by fluid-structure interaction. This phenomenon is a common denominator in every dynamic fluid-immersed structure. Therefore, transducing kinetic energy into a usable resource, such as electricity, is the key for a smart structure application.

Researchers have been able to do so using smart materials in flexible high aspect ratio wings. The concept of a wing with one Free-Floating Flap

(FFF) [1] is introduced for gust alleviation within flutter constraints. Later, a new aeroservoelastic approach based on FFF actuated by piezoelectric tabs [2] is proposed, evidencing superior effectiveness in gust alleviation and flutter suppression.

The concept was took into another level when an electromagnetic energy harvester was placed at the flap hinge to exploit flutter-induced Limit-Cycle Oscillations (LCO) [3], also numerically predicting the flutter speed controllability by varying the generator external load. This leads to the proposal of an autonomous flap for offshore wind turbines [4], which envisages an energetically self-sustainable plug-in control surface that harvests energy to power an active gust alleviation system. However, such energy requirements demand for large flap deflection and angular velocity. To boost the energy harvested, a gearbox is introduced though the inertial effects deeply downgrade the overall performance of the system.

As such, the purpose of this research is to develop a harvester able to increase the produced

energy by optimizing the rotational mechanism, proving it both numerically and experimentally. Moreover, the premise of flutter speed control is also investigated experimentally. In the end, the enhanced mechanism is subjected to a preliminary evaluation for future integration in airframes.

## 2. Methodology

The procedures presented hereafter aim to determine the feasibility of an energy harvesting mechanism to exploit flutter-induced vibrations by means of numerical and experimental simulations.

### 2.1. Numerical Methods

A numerical study is carried out to evaluate the mechanism feasibility. The physical reality is numerically described and two methods are used to calculate the instability boundary and time-domain response of the system. For the former, an eigenvalue problem in the frequency domain is solved based on the  $p$ - $k$  method to determine the flutter onset. Yet, and due to non-linear behavior of the new mechanism that allows for shaft free-spinning, a time-domain simulation is also performed. Afterwards, the code developed is benchmarked.

The numerical method is based on the theory presented by Theodorsen [5] and follows the notation introduced in his report on aeroelastic flutter idealized for a classical 3DOF spring-damper airfoil. As such, the equations of motion are exposed according to the following equation.

$$[\mathcal{M}]\{\ddot{\xi}\} + [\mathcal{C}]\{\dot{\xi}\} + [\mathcal{K}]\{\xi\} = \{\mathcal{Q}\} \quad (1)$$

where  $[\mathcal{M}]$  is the generalized inertia matrix,  $[\mathcal{C}]$  the damping matrix,  $[\mathcal{K}]$  the stiffness matrix,  $\{\mathcal{Q}\}$  the vector of generalized applied forces, and  $\{\xi\}$  the state vector.

Introducing a generator at the flap hinge introduces a non-usual damping term into the system. Hence, the electromagnetic damping value estimator  $C_{el}$  is added to a standard viscous damping model, considering it only affects the flap mode.

$$[\mathcal{C}] = [\mathcal{C}_{visc}] + \begin{bmatrix} 0 & 0 & 0 \\ 0 & 0 & 0 \\ 0 & 0 & C_{el} \end{bmatrix} \quad (2)$$

Considering a brushed permanent magnet Direct Current (DC) motor retro-used as a generator, the circuit may be modeled as depicted in Figure 1. Following such, the flap damping component is given by Equation 3 where  $GR$  is the gear ratio,  $\phi$  the induction coefficient and  $R_{eq}$  the resistance as seen from the generator's terminals.

$$C_{el} = \frac{(GR \cdot \phi)^2}{R_{eq}} \quad (3)$$

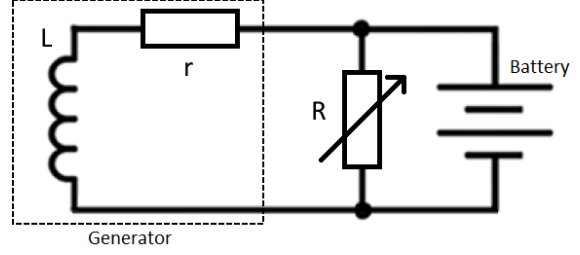


Figure 1: Electric circuit for energy harvesting

### Flutter Model

For flutter calculation purposes, the only external force applied to the system is related with its aerodynamics, modeled according to Theodorsen's theory for unsteady aerodynamics [5] as depicted in Equation 4. This fully defines the 3DOF system presented in Equation 1, using the  $p$ - $k$  method [6] to compute the aerodynamic matrices.

$$\{\mathcal{Q}\} = [\mathcal{M}_{aero}]\{\ddot{\xi}\} + [\mathcal{C}_{aero}]\{\dot{\xi}\} + [\mathcal{K}_{aero}]\{\xi\} \quad (4)$$

The final set of equations of motion with both structural and aerodynamic properties poses a Quadratic Eigenvalue Problem (QEP). It is possible to linearize the differential equation and reduce its order by introducing a new state variable  $\{\lambda\}$ , performing a First Companion Linearization (FCL). This origins a companion matrix  $[\mathcal{Z}]$  that gathers all the 3DOF system features. The eigenvalue problem is then solved according to Equation 5. Mode switching is avoided by using the Modal Assurance Criterion (MAC) and the flutter onset interpolated when one of the modes goes unstable.

$$([\mathcal{Z}] - p[I]) \begin{Bmatrix} \{\xi\} \\ \{\lambda\} \end{Bmatrix} = \{0\} \quad (5)$$

The algorithm is developed using Python<sup>®</sup> programming language. Benchmarking is performed for the 2DOF, 3DOF undamped and damped models. The latter is presented in Figure 2, showing that the output matches reference [7] and accurately predicts flutter for the heave mode.

### Time-Domain Model

Frequency-domain flutter detection algorithms may successfully detect the flutter boundary for complex systems but are unable to simulate the time response for underlying non-linear features as gearboxes, release mechanisms and electromagnetic decay of a rotating shaft.

Firstly, one should note that inertia only plays a role in flap motion when the system accelerates. For geared systems, the input shaft inertia is given by Equation 6, meaning that the larger the Gear Ratio, the larger the moment of inertia. Recent research has struggled in dealing with high gear ratios coupled to FFF [4], as it increases the flap

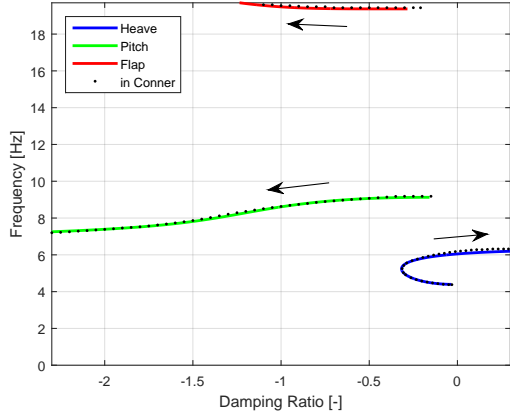


Figure 2: 3DOF damped system root locus plot

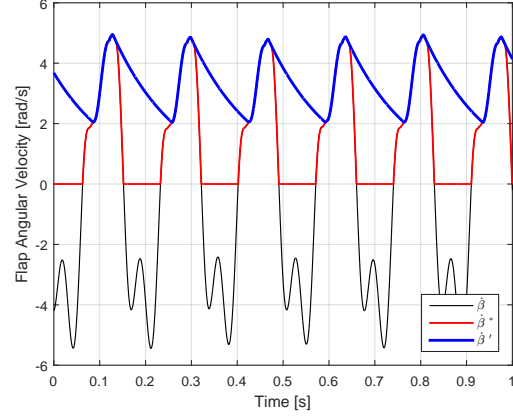


Figure 3: One-Way Bearing mechanism time response

#### Algorithm 1 Release Mechanism

```

1: procedure INERTIA DECOUPLING
2:   if  $\dot{\beta}(t) > \dot{\beta}(t-1)$  and  $\dot{\beta}(t) > 0$  then
3:      $I_{\beta} \leftarrow I_{flap} + GR^2 \cdot I_{GB}$ 
4:      $C_{el} \leftarrow \frac{(GR \cdot \langle \phi \rangle)^2}{R_{eq}}$ 
5:   else
6:      $I_{\beta} \leftarrow I_{flap}$ 
7:      $C_{el} \leftarrow 0$ 

```

#### Algorithm 2 Free-spinning shaft decay

```

1: procedure ELECTROMAGNETIC AND EFFICIENCY
   DECAY
2:    $\kappa \leftarrow \frac{C_{el}}{2I_{\beta}\omega_{\beta}} + 1 - \eta_{GB}$ 
3:   if  $\dot{\beta}^*(t) \leq \dot{\beta}^*(t-1)$  and  $\dot{\beta}'(t) > \dot{\beta}^*(t)$  then
4:      $\dot{\beta}'(t) \leftarrow \dot{\beta}'(t_0)e^{-\kappa(t-t_0)}$ 
5:   else
6:      $\dot{\beta}'(t) \leftarrow \dot{\beta}^*(t)$ 

```

shaft inertia. In order to avoid this feature, innovative mechanisms that reduce the influence of inertia and electromagnetic damping in the flap shaft shall be investigated.

$$I_{\beta} = I_{flap} + GR^2 \cdot I_{GB} \quad (6)$$

One of the possible solutions is a mechanism that somehow resembles the one of bicycles: a One-Way Bearing mechanism. It is, in fact, a bearing that only transmits the stroke in one direction, consisting of a release mechanism; when the shaft rotates in the opposite direction, the input to the generator free-spins according to an exponential decay  $\kappa$  ruled by the gearbox efficiency  $\eta_{GB}$  and electromagnetic damping. It can be modeled in time-domain according to Algorithms 1 and 2, and the resultant plot is depicted in Figure 3.

A more complex version, the Two-Way Bearing mechanism, is also developed, though the much simpler counterpart has better trade-off and therefore is chosen to pursue experimental validation. Likewise, a Standard version consisting of a reciprocating shaft directly connected to the generator is yet conceived.

As time marching is required to solve such problem, a state space model is developed. However, incorporating the frequency-domain complex aerodynamic matrices in that model lays out of the scope of this research. As such, a solution that equally represents the physical reality of the aerodynamic forces was applied - a harmonic function. In the end, the state space model based on the system of Equation 1 is presented as follows.

$$\begin{cases} \dot{X} \\ Y \end{cases} = \begin{bmatrix} A \\ C \end{bmatrix} \{X\} + \begin{bmatrix} B \\ D \end{bmatrix} \{u\} \quad (7)$$

where  $[A]$  is the state matrix,  $[B]$  the input matrix,  $[C]$  the output matrix, and  $[D]$  the feedthrough one;  $\{X\}$  is the state vector,  $\{u\}$  the input vector, and  $\{Y\}$  the output one. The time-domain simulation for the One-Way Bearing and Standard mechanisms is developed in Matlab/Simulink<sup>®</sup> R2015a and presented in Figure 4.

Time-domain results are verified against the time response based on the frequency-domain eigenvalues calculated using the flutter model for zero velocity. Figure 5 shows a snapshot of the time history for both methods with the same initial condition, which match.

## 2.2. Experimental Methods

An experimental setup to validate numerical predictions is developed in accordance with their geometric and structural inputs. Two test campaigns are planned: vibration and wind tunnel tests. The former aims to the structural characterization of the model by defining its resonance modes, and the latter focus on the flutter boundary and aeroelastic behavior. Both are used to test the energy harvesting performance by applying either forced harmonic vibrations in the vibration tests, or simply by performing a wind tunnel flutter test where the aerodynamic force may be approximated as a harmonic function.

The structural properties of the experimental model may be evaluated in Appendix A, Table A.1.

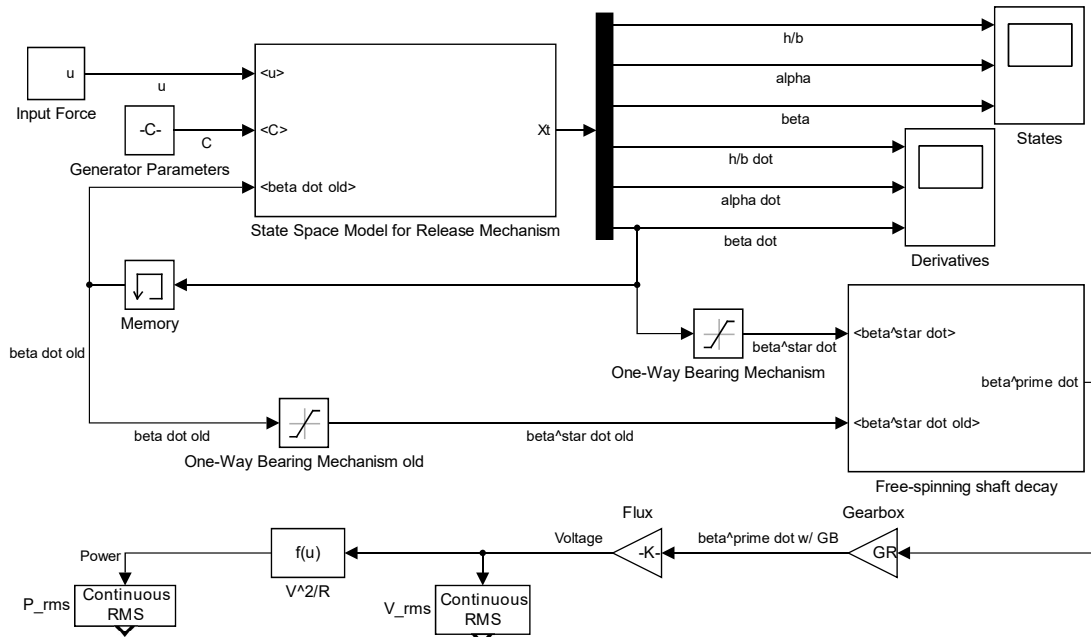


Figure 4: Matlab/Simulink<sup>®</sup> model for the One-Way Bearing mechanism

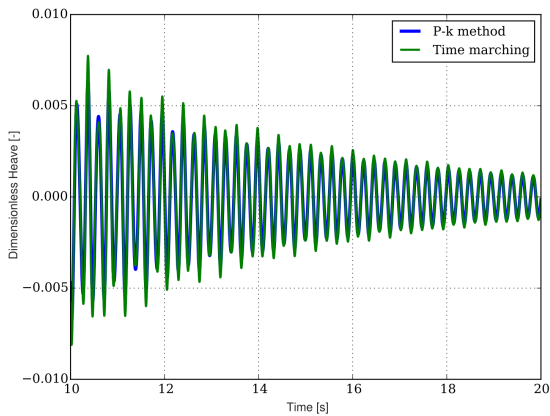


Figure 5: Time marching code benchmark with the  $p$ - $k$  method

### Test bench

The experimental framework used to test the energy harvesting mechanism is an acrylic wind tunnel test section with dimensions of  $0.35 \times 0.4 \times 1.0 \text{ m}^3$ . It holds a support system for a vertically-placed 2DOF rigid wing with integrated measuring systems [8]. This is then upgraded to fit a 3DOF aeroelastic model as described in the next section.

Data is acquired using an automated acquisition system consisting of a NI cDAQ-9172 chassis with two NI 9215 input modules and one NI 9263 output module. The experimental procedure automation is achieved using LabVIEW<sup>®</sup> 2017, as in Figure 6.

### Wing Model

The experimental model consists in a NACA 0024 profile with 240 mm chord and 360 mm diameter. The flap hinge is located at 72.5 % of the chord, with maximum thickness of 29 mm allowing to fit a generator at the hinge line. It is designed to house the whole energy harvesting setup, namely the re-

lease mechanisms which performance is to be assessed. Thereby, the assembly process is carefully engineered such that it would be possible to swap between mechanisms while maintaining the remaining system untouched.

The full system CAD model developed in CATIA<sup>®</sup> V5R21 may be evaluated in Figure 7. The generator may be seen in black, the One-Way Bearing mechanism in a golden color, and a connector between them in red. Note that the flap torsional spring system allows for two flap configurations: Setup I with some flap torsional stiffness and Setup II with none (FFF). Moreover, the measuring system of flap deflection uses a potentiometer to measure the flap shaft angle with respect to the main wing. In summary, all the systems in this concept were custom developed for this application.

The model is then manufactured using Formlabs<sup>®</sup> Form2 3D printer. As such, it was possible to engineer a lightweight skin-rib blended wing and completely model the concept to fit standard components as bearings, nuts, screws, and the generator itself.

Endplates with 1.2 times the chord length and almost 4 times the maximum airfoil thickness are manufactured using carbon-fiber reinforced polymer and attached during wind tunnel tests.

Calibration procedures are carried out to experimentally determine the model structural parameters, gathered in Table A1. In this procedure, by comparing damping introduced by each mechanism in the flap mode, one concludes that the One-Way Bearing mechanism decreases in 40 % the damping signature of the Standard solution.

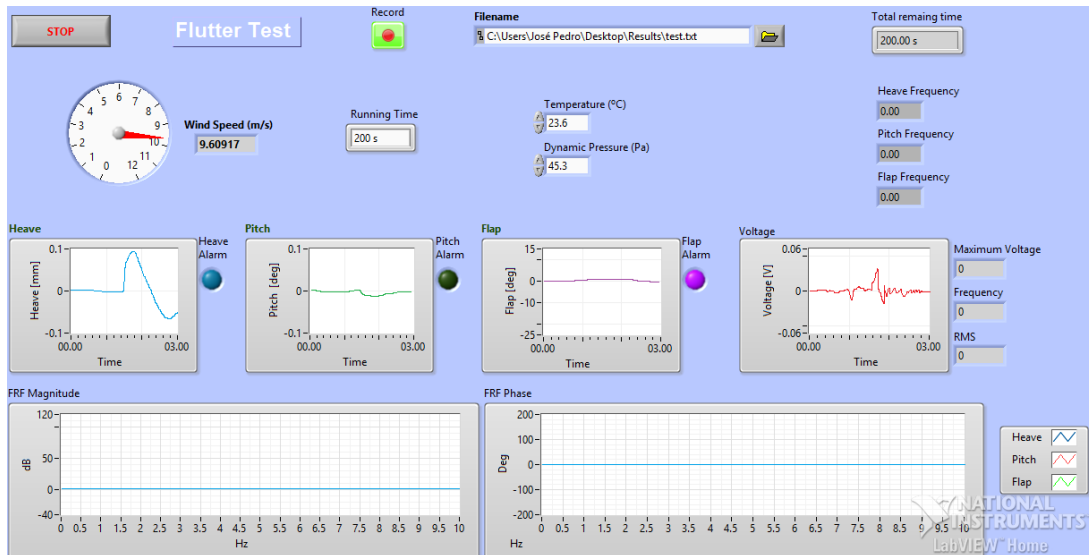


Figure 6: LabVIEW<sup>®</sup> graphical interface for the automated flutter test



Figure 7: Wing assembly CAD model (flap uncovered)

### Apparatus

The experimental test campaign starts with vibrations tests to structurally characterize the mechanisms by its resonance frequencies and assess the energy harvested for different resistance values.

Modal analysis of complex systems outputs the coupled natural frequencies for each vibration mode after an hammer-like impulse excitation. These modes fully characterize the model and enable the time-domain code validation by analyzing its time response. On the other hand, the energy harvesting capabilities are tested with a forced harmonic excitation emitted by an electromagnetic shaker in which a fully-automated frequency sweep will reveal the optimal condition for voltage production, as depicted in Figure 8. The mechanisms are then compared at that point. The procedure is carried out solely for the Setup I flap configuration.

Afterwards, experimental flutter tests are performed to determine the flutter onset and assess the energy harvesting mechanisms performance.

The test campaign is carried out in the low-speed W-Tunnel at Delft University of Technology, as seen in Figure 9. It is an open-jet wind tunnel facility with cross-section of  $0.4 \times 0.4 \text{ m}^2$  and maximum velocity of 35 m/s. The instability threshold is determined for different resistances as it influences

damping in the system, enhancing the flutter model code validation by estimating the damping associated to the experimental response. At the flutter point, the energy harvesting capabilities are tested in the same way as done for the vibration tests. Note that the energy harvesting procedure is carried out for both flap configurations. The virtual instrument developed to fully automate the data acquisition procedure is depicted in Figure 6.

### 3. Results & Discussion

This chapter focuses on the results obtained for the physical model data without gearbox. Experiments are planned in two different parts, both exciting the same feature: the limit-cycle behavior of the system. In the end, an application of such mechanism with a gearbox is studied with the validated time-simulation for an aeronautical case study. Discussion is structured around the main findings.

Data is acquired with a sampling frequency of 1 kHz. Post-processing is performed by applying a Lowpass Butterworth Filter with passband corner frequency of 30 Hz, stopband of 50 Hz, passband ripple of 1 dB and stopband attenuation of 25 dB to experimental data and using the Fast Fourier Transform (FFT) algorithm. The output is then conducted into a Savitzky-Golay Filter to reduce noise. The order and frame length of this filter is adjusted to achieve the smoothest output signal. The last step consists of calculating the Frequency Response Function (FRF) using the  $H_v$  estimator.

#### 3.1. Vibration Tests

Results for these tests are obtained by analyzing the signal in frequency domain using FFT. For inter-comparability purposes, the FRF is computed as an output-to-input ratio.

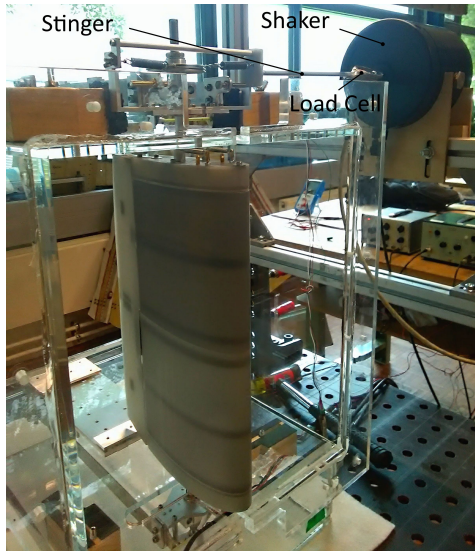


Figure 8: Forced harmonic excitation test setup

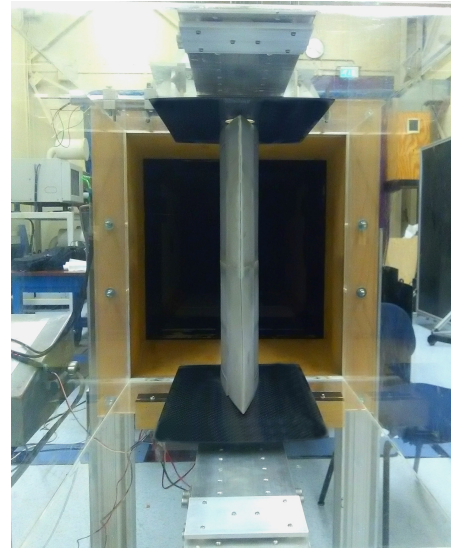


Figure 9: Wind Tunnel test section back view

### Validation of the Time-Domain Model

Validation is performed to verify the match between numerical experimental results. The simulation is run with experimental data for the input force, namely the magnitude read by the load cell during the experimental tests and the frequency given by the FFT applied to that signal. Time response of heave, pitch, and flap modes, alongside with voltage production are evaluated. Given the large combination of modes, mechanisms such as the Standard and One-Way Bearing, and circuit conditions as Open-Circuit (OC) and Short-Circuit (SC), only one validation case is presented in Figure 10.

Note that experimental responses are phase shifted with respect to the numerical output for easiness of interpretation. Apart from that, no further misalignment can be spotted, meaning that the numerical model accurately predicts the frequency output. With respect to the magnitude, it qualitatively estimates the experimental time response, despite over-predicting it by a range of 10 % to 15 %. This is most likely due to physical features not present in the model such as friction. Nonetheless, numerical results show very good agreement with the experimental ones, allowing for code validation.

### Modal Analysis

The system is excited with an impulsive force, a sharp peak that ideally excites all frequencies at wing's mid-span and close to the leading edge. The force is applied by a hammer-like structure with a rubbered tip and an incorporated load cell. Time history for left-to-right and right-to-left impulses is recorded to enrich the signal frequency range. 2DOF response is obtained for the flap locked with null deflection. The 3DOF time history is recorded for both mechanisms either OC or SC.

Figure 11 presents the experimental FRF for

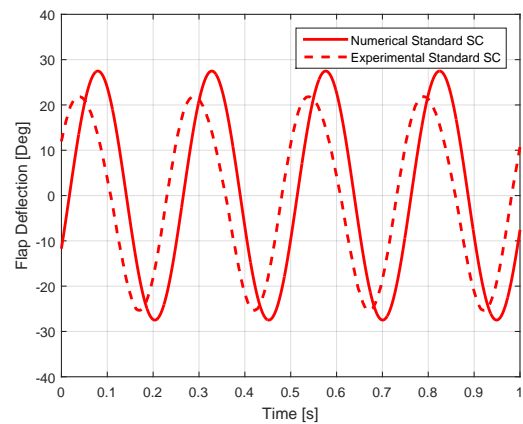
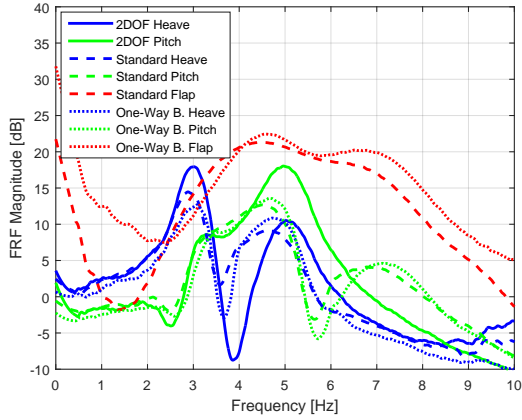


Figure 10: Flap time response

both mechanisms under OC conditions in 2DOF and 3DOF systems, clearly showing the effect of the third degree of freedom in the system and how mechanisms influence the system response.

For the 2DOF system, two distinct peaks are spotted at 3 Hz and 5 Hz at 17.5 dB FRF magnitude, respectively corresponding to heave and pitch coupled natural frequencies. With the introduction of the third degree of freedom, the peak drops below 15 dB and a slightly shifts to the left. Most importantly, a third peak appears around 7 Hz corresponding to the flap coupled natural frequency. Curiously, the pitch mode seems to also increase its amplitude at this resonance point whereas the heave mode completely drops. This same coupling occurs for heave and pitch modes at lower frequencies. Comparing these results with the uncoupled natural frequencies in Table A1, both coupled and uncoupled natural frequencies match for heave and pitch modes, whereas in the flap mode it is shifted to around 7 Hz.

It is worth noting that, with both mechanisms in OC conditions, the electromagnetic damping is



**Figure 11:** FRF for impulse excitation applied to Setup I in OC conditions

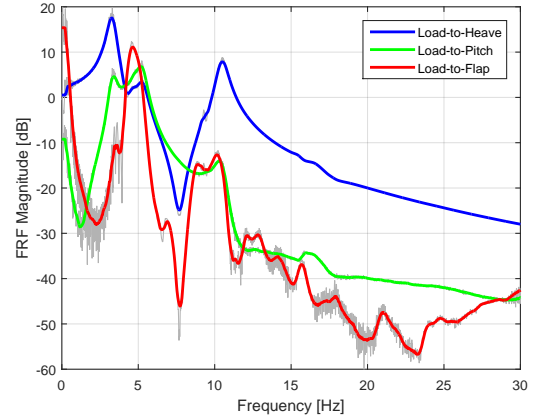


**Figure 12:** FRF for forced harmonic excitation applied to Setup I One-Way Bearing mechanism in OC conditions

minimal. Therefore, all measurements are strictly related with viscous damping. As experimentally determined for the uncoupled system in Section 2.2, the One-Way Bearing mechanism introduces less viscous damping than the Standard one. As a consequence, the resonance peak in the flap mode is larger and thinner. The same behavior is generally observed for the remaining modes.

Moreover, the same procedure is carried out in SC conditions. Results have shown the diminishing of resonance peaks, proving the increase of overall damping when the resistance is decreased.

### Energy Harvesting

The system is excited with a forced harmonic vibration in several frequencies to determine the optimal point for energy harvesting. This is done for both mechanisms, and corresponds to the frequency at which flap deflection is largest. The frequency sweep is first performed for a range of 30 Hz as in Figure 12, and then shortened to converge for the optimal values of 4.06 Hz for the Standard mechanism and 4.43 Hz for the One-Way Bearing.

At the optimal point, voltage is generated and the RMS of the signal positive stroke is performed in a 80-second time window to average the voltage into a *quasi*-DC value. The results are depicted in Figure 13 and clearly quantify the advantages of One-Way Bearing mechanism. In this Setup I flap configuration, it produces 20.5 % more voltage than the Standard one in OC conditions, and 25.0 % more power at maximum power condition around 10  $\Omega$ .

### 3.2. Wind Tunnel Tests

Results for flutter plots are obtained by using the least squares method to fit experimental time response with an exponentially damped harmonic curve. Data for the energy harvesting assessment is then gathered at the lowest velocity at which the system evidences LCO.

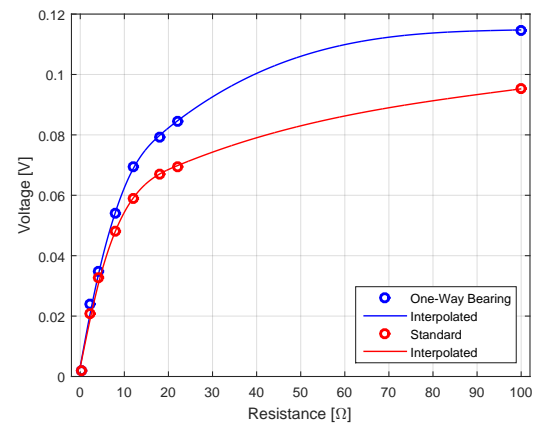


**Figure 13:** Voltage production for Setup I under forced harmonic excitation

### Validation of the Flutter Model

Validation of flutter code aims to verify the match between numerical and wind tunnel tests, with the simulation running for the structural properties in Table A1. Time response is recorded and damping ratio and frequency obtained after filtering the signal and performing curve fitting for both mechanisms, circuit conditions and flap configurations.

A validation example may be evaluated in Figure 14, where blue stands for heave and green for pitch. It evidences the electromagnetic damping added by increasing the damping ratio in SC conditions, though with a marginal decrease in flutter speed. In the end, it is possible to state that experimental results corroborate the numerical predictions, counting with a difference of 10.1 % and 9.2 % respectively for OC and SC conditions in flutter speed, and 6.5 % and 7.0 % in frequency. These are acceptable values for numerical flutter model validation which align with literature [7].

### Flutter Speed Control

Flutter speed controllability by changing the resistance at the generator terminals is hereafter experimentally tested in order to prove previous numerical predictions [3]. To do so, both flap configura-

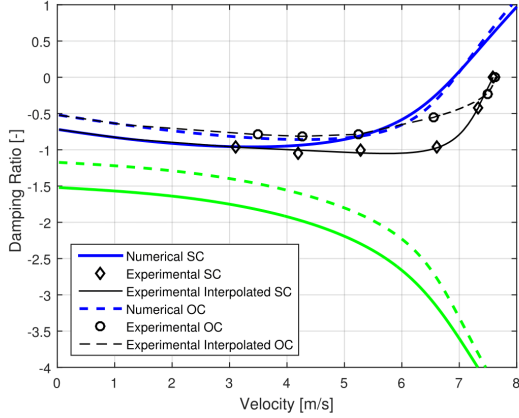


**Figure 14:** Heave-pitch flutter mechanism for the Setup I Standard mechanism

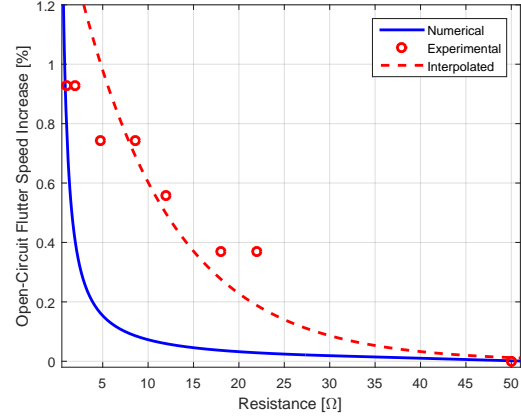


**Figure 15:** Flutter speed controllability for Setup II One-Way Bearing mechanism in OC conditions

tions and mechanisms are tested such that its flutter speed is compared with the numerical predictions for a wide range of resistances. Once more, only one case study is presented.

Experimental results in Figure 15 show a marginal but monotonic increase in flutter speed as damping increases, meaning that both numerical and experimental results follow an exponential relation, though with a much lower decay rate for the experimental case. Nonetheless, simulations have shown a much more controllable range of resistances. This has to do with the generator internal resistance of  $8 \Omega$  that limits the equivalent output resistance  $R_{eq}$  depicted in Figure 1.

Furthermore, and on the contrary of Setup II, experimental data showed that flutter speed has not increased for the same situation in Setup I, with this being also predicted by the flutter code. This means that only for the FFF configuration does the flutter velocity increases as initially thought. A thorough analysis to Setup II characteristics leads to a pretty unusual damping characteristic: the flap critical damping value is zero. Hence, by comparing total and critical damping values, one can conclude that Setup I is an underdamped system, whereas Setup II (FFF) is overdamped. This is a prominent finding, confirming FFF as active flutter speed controllers by means of changing its external load.

### Energy Harvesting

The system is forced into LCO at the flutter point and the voltage generated is evaluated according to the same procedure of vibration tests. This is done for both mechanisms and flap configurations, and over a wide range of external loads.

Experimental results show that Setup II One-Way Bearing mechanism produces 33.9 % more voltage in OC conditions and around 45.0 % more power than the Standard mechanism at the optimal resistance, as depicted in Figure 16. These results clearly outperform similar concepts using the same

energy harvesting technique [3]. Moreover, it was evidenced that Setup II can generate almost twice the power produced by Setup I, if compared the absolute maximum values. Furthermore, the power peaks obtained for both vibration and wind tunnel tests are approximately located at  $8 \Omega$ , the exact same value as the internal resistance for the generator, confirming the maximum power theorem.

### 3.3. Concept Applicability

In this final section, and after being evaluated as a energy harvesting system for wind turbine rotors, the concept applicability to aeronautical industry is evaluated as an additional power source for low-power UAV in order to develop either hybrid or full-electrical power solutions.

To do so, the verified time-domain model emulates the experimental model and introduces a gearbox with a ratio of 25:1. Simulations are run for the same input harmonic force as in vibration tests. It turned out that the mechanism is able to generate 4.1 V and produce 2.1 W of energy at an external load of  $8 \Omega$ , as depicted on Figure 17.

To simulate an aircraft application, the mechanism is considered to engage in non-critical flight stages as loiter, lasting for 45 min. It may either be placed in the ailerons, meaning that they would operate either as control surface and energy harvesting device; or slightly more inboard, such that the FFF may have no other function than harvesting energy. The energy produced by the generator sums up to 1.58 Wh, stored in a compliant LiPo battery weighting 13.8 g and with specific energy of 114.5 Wh/kg. Together with the generator, it poses a 11.6 % mass increment in the wind tunnel model when compared with one with no energy harvesting mechanism. In terms of aerodynamic efficiency, the FFF solution presents a  $C_L$  loss in the order of 2 % for low-amplitude LCO [3]. However, no studies have been done so far concerning the drag penalty of such mechanism. Nonetheless,

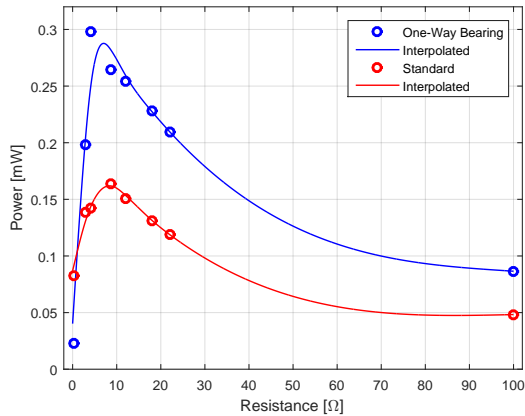


**Figure 16:** Power Generation for Setup II configuration at the flutter point

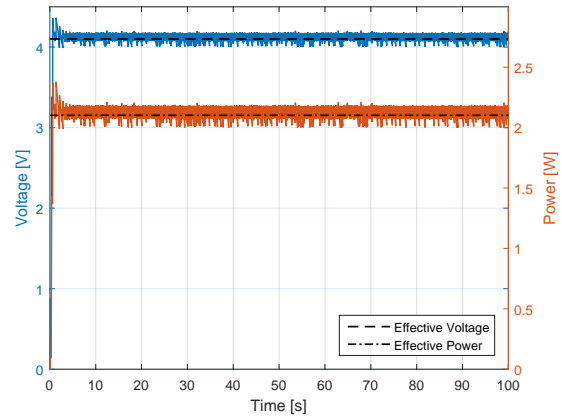


**Figure 17:** Numerical Simulation on Setup I One-Way Bearing mechanism with  $GR$  of 25

considering propeller-driven UAV powered by aviation gasoline, the mass of saved fuel is 0.115 g for the experimental model.

Future applications in larger aircraft are also of interest, as the NOVEMOR project emerges as a good testbed. Results have shown that a generator with 21.5 cm diameter would fit in the wing break point, leading to a 1.2 % penalty on the empty weight of the airframe. However, the remaining structural properties are not publicly available.

#### 4. Conclusions

A disruptive energy harvesting system with a release mechanism was numerically modeled, manufactured and experimentally tested during this research with the purpose of improving its performance, test the controllability of aeroelastic instabilities, and expand it to other areas of application.

This research has proved the usability of 3D-printed models in vibration and wind tunnel tests, in one of the first-ever flutter experiments using such manufacturing technique. Also, the numerical models developed were proved to be accurate in predicting the non-linear behavior of the system.

The accurate designing and manufacturing enhanced a 40 % reduction in viscous damping when compared to a standard reciprocating shaft. This poses a performance increase of 33.9 % in voltage and 45 % in power, for a mass penalty of 0.6 % of the wind tunnel model mass. Also, this research achieved the first experimental proof of the flutter speed controllability in overdamped systems.

Future applications in the aeronautical sector are numerically predicted, with estimated mass penalty of 11.6 % when compared with a model without energy harvesting mechanism, and promising fuel savings for increasingly larger gear ratios.

#### Acknowledgements

I would like to acknowledge Dr. J. Sodja and Prof. R. De Breuker from TU Delft, and Prof. A. Suleman

from IST for their thorough supervision and insightful guidance.

#### References

- [1] S. Heinze and M. Karpel. Analysis and wind tunnel testing of a piezoelectric tab for aeroelastic control applications. *Journal of Aircraft*, 43(6):1799–1804, 2006.
- [2] L. Bernhammer, R. De Breuker, M. Karpel, and G. Veen. Aeroelastic control using distributed floating flaps activated by piezoelectric tabs. *Journal of Aircraft*, 50(3):732–740, 2013.
- [3] L. Bernhammer, R. De Breuker, and M. Karpel. Energy harvesting for actuators and sensors using free-floating flaps. *Journal of Intelligent Material Systems and Structures*, 28(2):163–177, 2017.
- [4] L. Bernhammer, S. Navalkar, J. Sodja, R. De Breuker, and M. Karpel. Experimental and numerical investigation of an autonomous flap for load alleviation. *Journal of Aircraft*, pages 1–12, 2017.
- [5] T. Theodorsen. General theory of aerodynamic instability and the mechanism of flutter. *NACA Report 496*, pages 413–433, 1934.
- [6] H. Hassig. An approximate true damping solution of the flutter equation by determinant iteration. *Journal of Aircraft*, 8(11):885–889, 1971.
- [7] M. Conner, D. Tang, E. Dowell, and L. Virgin. Nonlinear behavior of a typical airfoil section with control surface freeplay: A numerical and experimental study. *Journal of Fluids and Structures*, 11(1):89 – 109, 1997.
- [8] B. Gjerek, R. Drazumeric, and F. Kosel. A novel experimental setup for multiparameter aeroelastic wind tunnel tests. *Experimental Techniques*, 38(6):30–43, 2014.

## Appendix A: Experimental System Properties

The system parameters presented hereafter are defined according Theodorsen aeroelastic 3DOF model [5].

Table A1: Wing Model Properties

	Constant	Vibration Tests	Wind Tunnel Tests	Standard Mechanism	One-Way Bearing Mechanism
<b>Geometric Properties</b>					
Span [m]	0.36				
Chord [m]	0.24				
Semi-chord, $b$ [m]	0.12				
Elastic Axis, $a$ (w.r.t. $b$ ) [-]	-0.20				
Hinge Line, $c$ (w.r.t. $b$ ) [-]	0.45				
<b>Stiffness Properties</b>					
Heave Stiffness, $K_h$ [N/m]	676.1				
Pitch Stiffness, $K_\alpha$ [Nm/rad]	4.240				
Flap Stiffness, $K_\beta$ [Nm/rad]	<b>Setup I: 0.178</b> <b>Setup II: 0.0</b>				
<b>Damping Properties</b>					
Heave Damping, $C_h$ [Ns/m]		2.3547	1.7564		
Pitch Damping, $C_\alpha$ [Nms/rad]		$1.6360 \times 10^{-2}$	$1.3489 \times 10^{-2}$		
Flap viscous damping, $C_\beta$ [Nms/rad]				$1.7457 \times 10^{-3}$	$1.0543 \times 10^{-3}$
Generator Induction Coefficient, $\phi$ [Vs/rad]	$1.8741 \times 10^{-2}$				
<b>Inertia Properties</b>					
Wing Mass, $m$ [kg]		1.2137	1.3777		
Support Mass, $m_s$ [kg]	0.6293				
Pitch Static Moment, $S_\alpha$ [kgm]		$2.9639 \times 10^{-2}$	$3.7793 \times 10^{-2}$		
Pitch Inertia Moment, $I_\alpha$ [kgm <sup>2</sup> ]		$4.8620 \times 10^{-3}$	$7.2199 \times 10^{-3}$		
Flap Static Moment, $S_\beta$ [kgm]		$8.4823 \times 10^{-3}$	$9.6285 \times 10^{-3}$		
Flap Inertia Moment, $I_\beta$ [kgm <sup>2</sup> ]				$1.7481 \times 10^{-4}$	$1.5646 \times 10^{-4}$
Wing CG distance from $a$ , $x_\alpha$ (w.r.t. $b$ ) [-]		0.2035	0.2286		
Flap CG distance from $c$ , $x_\beta$ (w.r.t. $b$ ) [-]	$5.824 \times 10^{-2}$				
Heave Natural Frequency, $\omega_h$ [Hz]		3.0486	2.9242		
Pitch Natural Frequency, $\omega_\alpha$ [Hz]		4.7000	3.8569		
Flap Natural Frequency, $\omega_\beta$ [Hz]				5.0786	5.3681